Facile *in Situ* Synthesis of BiOCl Nanoplates Stacked to Highly Porous TiO₂: A Synergistic Combination for Environmental Remediation

Miguel Guerrero,*,[†] Ainhoa Altube,[‡] Eva García-Lecina,*,[‡] Emma Rossinyol,[§] Maria Dolors Baró,[†] Eva Pellicer,*,[†] and Jordi Sort[∥]

[†]Departament de Física, Facultat de Ciències, Universitat Autònoma de Barcelona, E-08193 Bellaterra, Spain

[‡]Surfaces Division, IK4-CIDETEC, Paseo Miramón, 196, E-20009 San Sebastián, Spain

[§]Servei de Microscòpia, Universitat Autònoma de Barcelona, E-08193 Bellaterra, Spain

[∥]Institució Catalana de Recerca i Estudis Avançats (ICREA) and Departament de Física, Universitat Autònoma de Barcelona, E-08193 Bellaterra, Spain

ABSTRACT: A novel nanocomposite material made of two-dimensional BiOCl nanoplates assembled into highly porous titania has been successfully prepared following a facile sol–gel reaction. Both the TiO₂ (anatase) and BiOCl components are crystalline as demonstrated by X-ray diffraction and transmission electron microscopy analyses. TiO₂ exhibits a highly porous network and possesses a small crystallite size, whereas BiOCl forms micrometer-sized plates with nanometer thicknesses. Aqueous photocatalytic activity tests with this novel material have been performed on photodegradation of Rhodamine B under ultraviolet–visible light irradiation. Interestingly, the attachment of the BiOCl nanoplates to the TiO₂ network significantly enhances the photocatalytic activity of the material compared to that of pure TiO₂ due to the formation of BiOCl/TiO₂ heterojunctions. Thus, this pertinent synergistic combination of TiO₂ and BiOCl proves to be a promising strategy for the large-scale production of a new generation of photocatalysts with excellent properties for the degradation of organic pollutants.

KEYWORDS: *porous TiO₂, nanocomposite, BiOCl, photocatalysis*
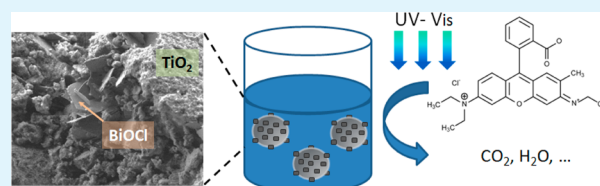
1. INTRODUCTION

Photocatalytic degradation as a wastewater treatment represents a promising approach for "green" environmental remediation.[1−3] Since Fujishima and Honda reported in 1972 the use of titanium dioxide as an electrode,[4] TiO₂ has become one of the most commonly used photocatalysts for the treatment of organic pollutants in water because of its chemical inertness, photostability, low-cost fabrication, and nontoxicity.[5−7] When illuminated with appropriate light sources in aqueous solutions, the photocatalyst generates electron–hole pairs, which initiate different chemical reactions and, therefore, produce the hydroxyl radical (OH•) and superoxide anions (O²⁻) responsible for the photoactivity.[8] However, as a semiconductor with a large band gap (~3.2 eV; λ_{ex} < 380 nm), TiO₂ presents a relatively low quantum efficiency in the visible wavelength range that limits its outdoor application (only 4% of the solar spectrum). Also, a high recombination rate of photoinduced electron–hole pairs often occurs in TiO₂ because of the overlap between the excitation and emission bands.

From the viewpoint of practical use, in the past several years great effort has been spent to improve the photocatalytic efficacy of TiO₂ by doping it with suitable secondary components. This makes the resulting material appealing for clean, affordable, and abundant solar energy.[9] Many reports have shown how the photocatalytic properties of TiO₂ can be significantly influenced by the addition of different amounts of metallic or metal oxide species.[10−13] Interestingly, there have been several studies of the photocatalytic properties of Bi-doped TiO₂ composites under ultraviolet (UV)–visible light irradiation.[14−16] At the same time, bismuth oxychloride (BiOCl), considered one of the most important bismuth oxyhalides, has also attracted an enormous amount of attention within the scientific community because of its excellent catalytic and photoluminescent properties,[17] hence finding numerous uses as a photocatalyst.[18−20] BiOCl crystallizes in the P4/*nmm* tetragonal space group and has a layered structure consisting of [Cl−Bi−O−Bi−Cl] sheets held together by the nonbonding interaction through the Cl atoms along the *c*-axis.[21] Among all the different BiOCl nanostructures, two-dimensional (2D) BiOCl nanoplates and nanosheets are greatly important because they typically exhibit high crystallinity, large surface areas, and structural anisotropy. However, this material is still hard to synthesize, and developing it through an environmentally friendly route remains a challenge. Because of the properties of BiOCl and TiO₂, it is envisaged that a nanocomposite consisting of these two materials could hold promise for advanced photocatalytic applications. Additionally,

compared to the bulk, porous TiO_2 (PT) could be potentially beneficial for enhancing the diffusion of reactants and, as a consequence, enhancing the photocatalytic activity.[22−27]

In this study, we report for the first time a direct and facile growth method that yields 2D BiOCl nanoplates assembled into a highly porous TiO_2 network (BiOCl-PT) and its characterization. This system exhibits a powerful and efficient aqueous photocatalytic activity under UV−visible light irradiation for the degradation of Rhodamine B (RhB), proving the synergetic effect between BiOCl and TiO_2.

2. EXPERIMENTAL SECTION

2.1. Sample Preparation. A two-step hydrothermal synthesis route was conducted to produce the $BiOCl/TiO_2$ nanocomposite. In brief, 10 mL of tetrabutyl orthotitanate $\{Ti[O(CH_2)_3CH_3]_4$, Aldrich, 97%$\}$ was dissolved in 50 mL of n-butyl alcohol, and then the solution was added dropwise to 40 mL of distilled water at pH 2 (using nitric acid, Aldrich, 69%). After the reaction mixture had been continuously stirred for 10 h at room temperature, a first hydrothermal treatment was applied in a sealed container at 80 °C for 4 h. In another beaker, 3.7 g of P123 $\{HO(CH_2CH_2O)_{20}[CH_2CH(CH_3)-O]_{70}(CH_2CH_2O)_{20}H$, BASF, 99%$\}$ was dissolved in 50 mL of distilled water. The TiO_2 precursor solution, once cooled to around 50 °C, was added dropwise to the P123 solution at 50 °C while being vigorously stirred. Immediately afterward, a solution containing 2.7 g of $BiCl_3$ in 100 mL of 1.2 M HCl was also added dropwise. The resulting mixture was stirred at 50 °C for 2 h, so that the P123 micelles could fully interact with the TiO_2 seeds and the BiOCl. Finally, a second hydrothermal treatment was conducted at 100 °C for 20 h. The resultant white powder was recovered by evaporation of the solution at 75 °C, introduced in a crucible, and then placed in a tubular furnace for calcination. The furnace temperature was increased to 450 °C at a rate of 1 °C min^{-1} and held at this temperature for 4 h under atmospheric conditions. At the end of this process, the furnace was slowly cooled to room temperature, and the resulting BiOCl-PT composite was collected. For the purpose of comparison, pure porous titania (PT) was also synthesized, following nearly the same synthetic procedure, except for the addition of the $BiCl_3$ compound.

2.2. Characterization. The morphology and chemical composition of the materials were investigated by high-resolution transmission electron microscopy (HRTEM) using a Jeol-JEM 2011 system operated at 200 kV and field emission scanning electron microscopy (FE-SEM) using a Merlin Zeiss microscope operated at 2 kV, equipped with energy dispersive X-ray (EDX) compositional analysis. Samples for TEM observations were prepared by dispersing a small amount of powder in ethanol, and then one or two drops of the suspension were placed onto a holey carbon grid. For FE-SEM characterization, the powders were spread onto carbon tape and directly imaged under the electron beam. Specific surface area analyses were performed using a Micrometrics Tristar 3000 instrument at 196.15 °C after the powders had been degassed at 135 °C for 1 h and subsequently at 350 °C for 4 h. Wide-angle X-ray diffraction (XRD) patterns were collected on a Philips X'Pert diffractometer in the 2θ range of 20−80° (step size of 0.03°, step time of 10 s) using Cu Kα radiation. The structural parameters (crystallite size, microstrains, and cell parameter) were evaluated by fitting the full XRD patterns using the "Materials Analysis Using Diffraction" (MAUD) Rietveld refinement software.[28−30] The MAUD software uses the Rietveld method to obtain structural information about the sample by fitting the entire XRD pattern, thereby overcoming the problem of peak overlap and allowing the maximal amount of information to be extracted. For crystallite size and microstrain determination, MAUD used the Delft model.[31,32] Crystallite sizes and microstrains are determined from the pure diffraction profile, $f(x)$. A good approximation of $f(x)$ is obtained using a Voigt function, which can be written as a combination of a Cauchy (related to crystallite size) and Gaussian (related to microstrains) functions. The program can also quantify stacking faults, based on Warren's formulas.[33] Thermogravimetric (TGA) and

differential scanning calorimetric (DSC) (TGA 7 and DSC 7, respectively; PerkinElmer) analyses were conducted under an air atmosphere, at a rate of 10 K min^{-1} from 25 to 500 °C. The sample weight was ∼10 mg.

2.3. Evaluation of Photocatalytic Activity. The photocatalytic activity of the materials (PT, BiOCl-PT, and commercial BiOCl) was evaluated by decolorization of a 10 ppm Rhodamine B (RhB) aqueous solution (Alfa Aesar, 98%, without further treatment). RhB was selected as model organic dye as it is one of the most common xanthene dyes in the textile industry, presents good stability as a dye laser material, and is used as a biological stain. RhB is highly soluble in water and organic solvents, and its color is fluorescent bluish red. The photodegradation of RhB is important with regard to the purification of dye effluents. Solutions were prepared by adding 0.3 g L^{-1} catalyst to be tested to 10 mL of the RhB solution. In addition to this, in each experiment, a blank RhB solution (without catalyst) was used as a control and reference test. The reaction cells were placed in a SwiftCure IB-450 irradiation cabin equipped with a mercury lamp. Following the recommendations given by the ISO 10678:2010 standard, suitable cutoff filters were used to limit the wavelength radiation and avoid direct photolysis of the dye. The average light intensity used was 220 W, and the wavelength ranged from 320 to 500 nm. The photocatalytic experiments were conducted under continuous magnetic stirring at a constant temperature of 29 °C.

After the suspensions had been conditioned for 40 min in dark to reach adsorption−desorption equilibrium, the light was turned on to initiate the reaction. Experiments were then conducted under UV irradiation for an overall time of 180 min. The red color of the solution faded gradually with time because of the decomposition of RhB. Aliquots were withdrawn regularly (at 0, 15, 30, 60, 120, and 180 min) from the reaction, and the dispersed powder particles were removed with a centrifuge. The supernatant solutions were then tested with a UV−vis spectrophotometer (Shimadzu UV-1603) by measuring absorption spectra of RhB ($\lambda = 554$ nm) as a function of irradiation time. The photocatalytic activity of the catalysts was calculated as C/C_o, where C_o is the concentration of the test solution of RhB before irradiation and C is the concentration of RhB after irradiation. The optical diffuse reflectance spectra were measured at room temperature using the same UV−vis instrument equipped with an integrating sphere attachment using NaF as a reference.

3. RESULTS AND DISCUSSION

3.1. Morphological and Structural Characterization. Thermogravimetric analysis (TGA) and differential scanning calorimetry (DSC) were performed on the reaction mixture prior to calcination to evaluate the temperature at which TiO_2 begins to crystallize and P123 is removed (Figure 1). Between 100 and 120 °C and between 135 and 185 °C, small
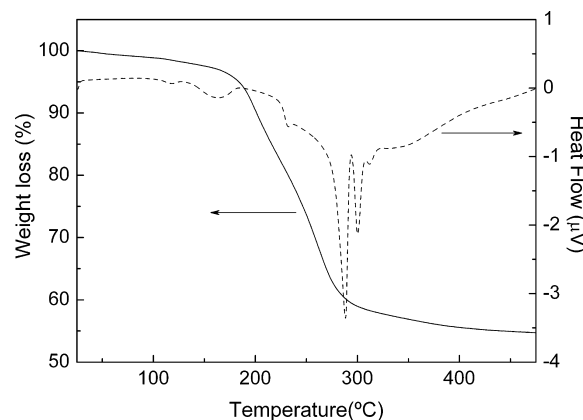
Figure 1. TGA (—) and DSC (⋯) data for the BiOCl-PT precursor at 10 K min^{-1}.

endothermic peaks are detected as a result of the evaporation of water and butanol (solvent from the synthesis), respectively. The TGA curve shows a decrease in mass of ≈5% at 170 °C. Two endothermic peaks appear around 288 and 300 °C, which correspond to the oxidation of the block copolymer agent (P123) and the formation of TiO_2. This is accompanied by a further decrease in the TGA curve of ≈37% in mass. Therefore, a calcination temperature of 450 °C was selected to ensure both the transformation of the precursor into TiO_2 and the complete removal of the P123 template. Higher temperatures were not considered to avoid BiOCl decomposition.[34]

X-ray diffraction (XRD) analysis was conducted to investigate the crystallographic structure of the prepared samples. XRD patterns of (a) pure porous TiO_2 (PT), (b) commercial BiOCl (for the purpose of comparison), and (c) BiOCl/TiO_2 nanocomposite (BiOCl-PT) samples are shown in Figure 2. As expected, the most predominant phase in curve a is
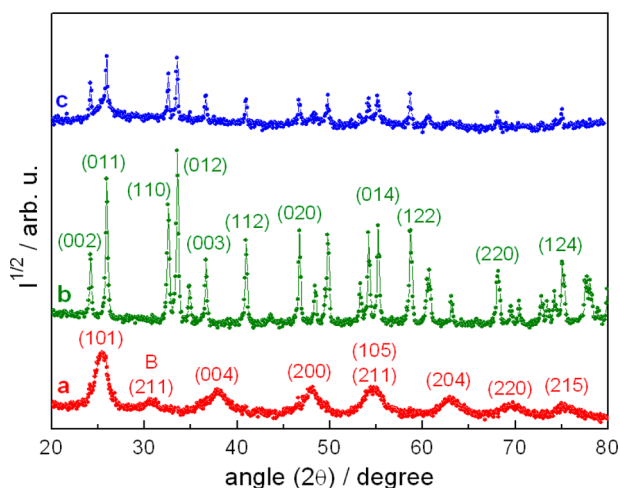
the BiOCl-PT nanocomposite and the lack of appreciable chemical reaction between BiOCl and TiO_2 components. The full XRD patterns were Rietveld fitted, and the crystallite size (average size of the coherent scattering domain) and microstrains for each phase are listed in Table 1. The crystallite

Table 1. Average Crystallite Sizes and Microstrains for Each Phase Present in the XRD Patterns of PT, Commercial BiOCl, and BiOCl-PT Samples Determined by Rietveld Fitting

sample	phase	$\langle D \rangle$ (nm)	$\langle \varepsilon^2 \rangle^{1/2}$ ($\pm 10^{-4}$)
PT	TiO_2 anatase	11 ± 2	6×10^{-3}
	TiO_2 brookite	7 ± 2	8×10^{-3}
commercial BiOCl	BiOCl	150 ± 10	8×10^{-4}
BiOCl-PT	TiO_2 anatase	8 ± 2	5×10^{-3}
	BiOCl	120 ± 10	5×10^{-3}

sizes for the TiO_2 component are in the range of 7−11 nm for both PT and BiOCl-PT samples, whereas the crystallite size of the BiOCl phase in BiOCl-PT sample is much larger (120 nm) and comparable to that of commercial BiOCl powder.

FE-SEM imaging was used to study the surface morphology of the BiOCl-PT composite. Figure 3 shows images of the BiOCl-PT composite particles at different magnifications. The composite particles are rather large, being tens of micrometers in size (Figure 3a). The arrows point to a few BiOCl nanoplates that are visible from the outer surface of a particle. The BiOCl nanoplates are strongly stacked to the highly porous TiO_2 network, as shown in Figure 3b, not only to the outermost

Figure 2. XRD patterns of (a) porous TiO_2 (PT), (b) commercial BiOCl, and (c) BiOCl/TiO_2 nanocomposite (BiOCl-PT) samples. Note that B denotes the brookite phase.

tetragonal anatase (JCPDS Card No. 84-1286), along with a small contribution of the brookite phase (JCPDS Card No. 76-1937), as noted from the presence of a reflection located at 30.7°. The peaks are rather broad, confirming the nanocrystalline nature of the sample. Commercial BiOCl (curve b) exhibits the typical pattern for pure tetragonal BiOCl (JCPDS Card No. 06-0249), featuring sharp and narrow reflections. The as-prepared nanocomposite (curve c) consists of a mixture of TiO_2 anatase and BiOCl phases. Some of the BiOCl reflections are superimposed to the anatase peaks. The peaks located at 24.2°, 34.8°, and 36.6° on curve c correspond to the (002), (012), and (003) crystalline planes of the BiOCl structure, respectively. These peaks are characteristic of lamellar structures. Moreover, all the BiOCl reflections are rather narrow, as for the commercial BiOCl powder, thus confirming the presence of well-crystallized BiOCl in the composite as well as its favored growth along the [110] orientation to form very thin layers.[35] No other phases have been found in the XRD pattern of the BiOCl-PT nanocomposite. Interestingly, the brookite peak located at 30.7° is no longer visible, which suggests that the TiO_2 component consists of only the anatase phase. Actually, a decrease in the amount of the brookite phase has been observed in doped TiO_2 powders compared to that in pure TiO_2.[12] The obtained results prove both the high purity of
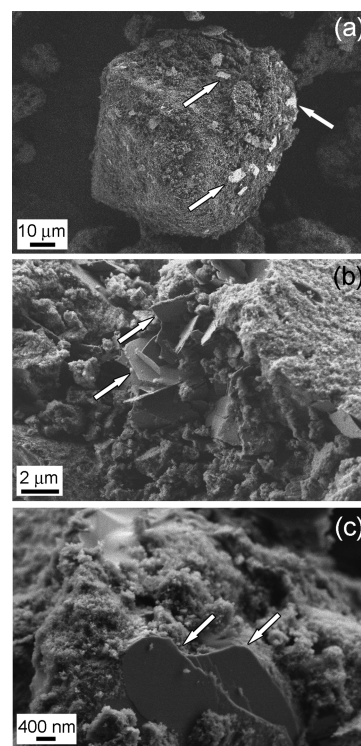

Figure 3. FE-SEM images of the BiOCl-PT composite showing (a) a typical composite particle and (b and c) magnified details of the composite particles in which the highly porous character of the TiO_2 material and the distribution and shape of the BiOCl nanoplates can be appreciated. The arrows point to BiOCl nanoplates stacked to the TiO_2 network.

surface of the particles but also to their interior. As shown in Figure 3c, TiO$_2$ is highly porous and the BiOCl nanoplates have widths ranging from 1 to 4 μm and thicknesses ranging from 100 to 300 nm. EDX mapping (Figure 4) shows the
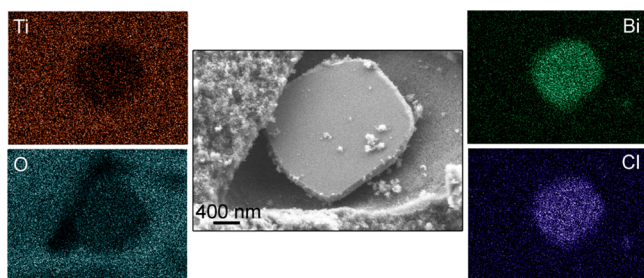

Figure 4. EDX mapping distribution of Ti, O, Bi, and Cl elements taken on a detailed region of the BiOCl-PT composite.

presence of titanium coming from the TiO$_2$ framework as well as bismuth and chlorine elements coming from the BiOCl nanoplates. The oxygen signal is larger in the TiO$_2$ region. The atomic ratio between Bi and Ti is ~0.3, which is close to the atomic ratio of the precursor solution.

HRTEM provided additional structural information concerning the *in situ* growth of the BiOCl nanoplates within the titania network. Panels a and b of Figure 5 reveal that the as-prepared nanocomposite is composed of well-distributed 2D BiOCl nanoplates well assembled into the porous TiO$_2$ structure. A close-up image of a single BiOCl nanoplate reveals its high crystallinity (Figure 5c), and the same holds for the TiO$_2$ network (Figure 5e). The selected area electron diffraction (SAED) pattern acquired from an individual BiOCl nanoplate (Figure 5d) shows a regular and clear square diffraction spot array with lattice spacings matching those of (113) and (012) planes, demonstrating the existence of the BiOCl tetragonal structure, which, in turn, is in agreement with the XRD results. The SAED pattern taken on the TiO$_2$ regions (Figure 5f) shows diffused lattice fringes, with an interplanar distance of 0.34 nm corresponding to the (101) *d* spacing of anatase TiO$_2$, confirming its nanocrystalline nature. Furthermore, it is clearly seen that the BiOCl has grown into close contact with the TiO$_2$ matrix, providing a tightly packed heterojunction structure.

The specific surface area of pure TiO$_2$ (PT) is 161 m^2 g^{-1} and decreases slightly to 117 m^2 g^{-1} when BiOCl is stacked to the TiO$_2$ network. This can be ascribed to the presence of the nonporous oxychloride chunks that partially shield the porosity of TiO$_2$. Nevertheless, the BiOCl-PT nanocomposite has a surface area more than 2 times larger than that of the commercial titania termed Degussa P25 (56 m^2 g^{-1}).[36] Such BiOCl-PT structure with a large surface area and three-dimensional connected pore framework could play an important role in catalyst design because of their potential capacity to improve the molecular diffusion of reactants and products.

3.2. Photocatalytic Activity. The photocatalytic performance of the materials was evaluated by comparing the degradation rate of RhB under UV−visible light irradiation (320 nm < λ < 500 nm) at a working temperature of 29 °C, after the adsorption−desorption equilibrium was reached (Figure 6).

As shown in Figure 6 (red line), the concentration of RhB decreases linearly with time in the presence of PT, reaching a removal ratio of 64% after exposure for 3 h. With regard to
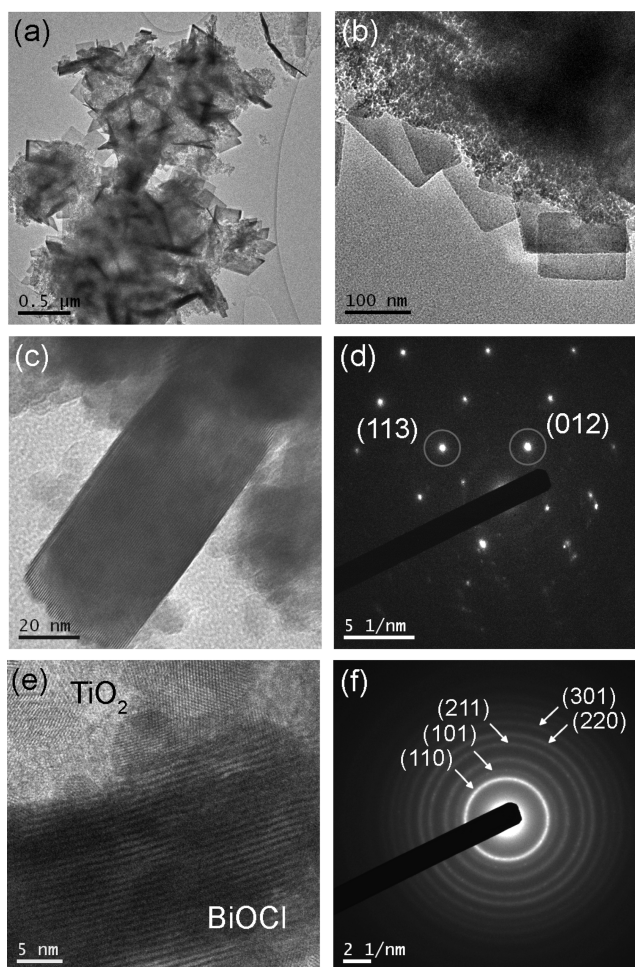

Figure 5. (a and b) HRTEM images at different magnifications of the BiOCl-PT composite. HRTEM image of (c) an individual BiOCl plate and (d) its corresponding SAED pattern. HRTEM image of (e) the TiO$_2$ region and (f) its corresponding SAED pattern.
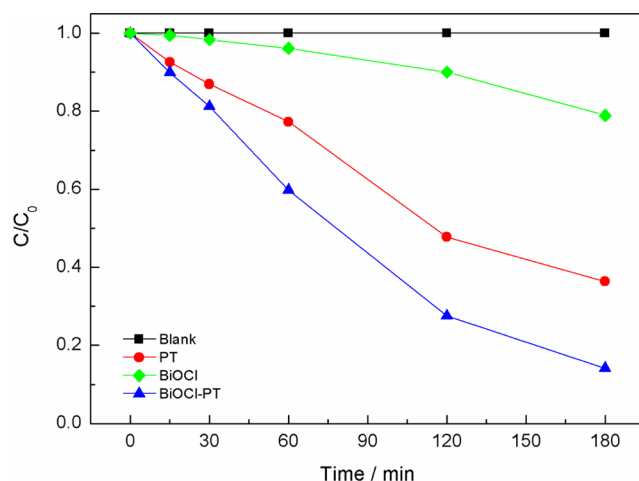

Figure 6. Decrease in RhB concentration over time of the pure RhB aqueous solution (black) in the presence of PT (red), BiOCl (green), and BiOCl-PT (blue) photocalysts.

commercial BiOCl, the photoactivity of this compound is lower than that of TiO$_2$; i.e., a maximal removal ratio of 21% was attained after the same exposition time (Figure 6, green line). This low photodegradation activity is probably due to both the

wide band gap of BiOCl[37] (∼3.29 eV) and its low solubility and porosity. Interestingly, BiOCl-PT (Figure 6, blue line) shows a photoactivity higher than those of PT and BiOCl because the concentration decay after 3 h is 86%. A control test without catalysts (Figure 6, black line) under UV−visible light irradiation showed that the photolysis of RhB was negligible in their absence.

The rate constants for the degradation of RhB in the presence of PT and BiOCl-PT were determined, assuming pseudo-first-order reaction kinetics[38,39]

$$\ln\left(\frac{C}{C_0}\right) = -kt \tag{I}$$

where k is the rate constant. The values of k were derived from the slope of plots of $\ln(C/C_0)$ versus time (t) shown in Figure 7. As shown in the figures, the fitting of experimental data gives
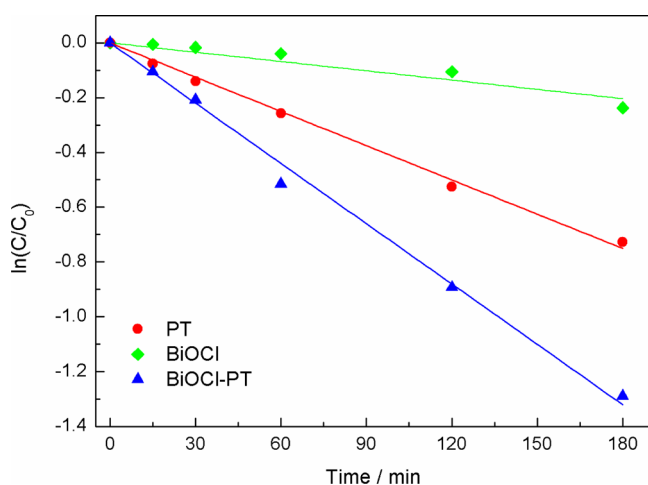

Figure 7. Plot of $\ln(C/C_0)$ of RhB concentration vs time for PT (red), BiOCl (green), and BiOCl-PT (blue) photocatalysts. The slope of the fitted line refers to rate constant k.

Table 2. Obtained Values of Rate Constants

sample	k (min^{-1})
PT	0.0042
BiOCl	0.0011
BiOCl-PT	0.0073

a good correlation. The determined rate constants (Table 2) confirm the enhanced reactivity of BiOCl-PT compared to those of PT and BiOCl. Our results are in agreement with those of Cai et al., who also observed an enhancement of the photocatalytic activity toward methyl orange and pentachlorophenol in BiOCl nanosheets grafted onto TiO$_2$ tubular arrays.[40] The rate constant of our BiOCl-PT sample is higher than that observed in the degradation of RhB using nanocrystalline TiO$_2$-zeolite composites with similar surface areas and TiO$_2$ crystallite sizes (k = 0.0040−0.0057 min^{-1}).[41] The same is true when the comparison is made with single-phase BiOCl. For example, BiOCl nanowire arrays exhibited a rate constant (k) of 0.0067 min^{-1} in the decomposition of RhB,[42] which is an interesting result bearing in mind that the BiOCl plates of our work have comparatively larger crystal sizes.

According to the BET results previously reported, the enhancement of the photocatalytic activity of BiOCl-PT cannot be ascribed to an increase in the specific surface area (which decreases for BiOCl-PT compared to that of PT). On the other hand, the change in the crystalline structure from a brookite/anatase mixture (PT) to almost only anatase (BiOCl-PT) should also be detrimental to the catalytic activity.[43] Instead, the observed higher efficiency of the decomposition of RhB can be mostly attributed to the formation of a heterojunction between the two components of the catalyst, BiOCl and TiO$_2$.[44] The decrease in the crystal size of the anatase TiO$_2$ from 11 to 8 nm in the composite could also exert a positive effect. It is known that the photocatalytic activity is sensitive to the crystallite size; higher activities are typically achieved for smaller crystal sizes.[45−47] Scheme 1 shows the most probable

Scheme 1. Most Probable Relative Energy Band Positions between Bulk BiOCl and TiO$_2$^{a}
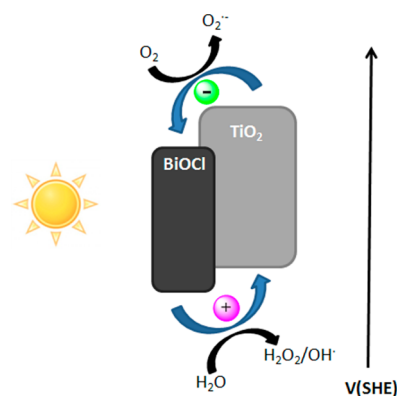
^{a}SHE denotes the standard hydrogen electrode. Photogenerated electrons (−, green) and photogenerated holes (+, purple).

relative energy band positions between bulk BiOCl and TiO$_2$.[48] Both the conduction band minimum and valence band maximum of BiOCl are more positive than those of TiO$_2$. Under light irradiation, electron−hole pairs can be produced in both BiOCl and TiO$_2$. Because of the driving force that arises from the difference between the conduction band edges of the two semiconductors, the electrons in TiO$_2$ are transferred to BiOCl [photogenerated electrons, e_{pg}^- (− in Scheme 1)]. Later, the holes [photogenerated holes, h_{pg}^+ (+ in Scheme 1)] in BiOCl are guided toward TiO$_2$ because of the difference between the valence band edges of the two semiconductors. Therefore, the heterostructures created in the BiOCl-PT nanocomposite probably favor the separation of electrons and holes, together with the inhibition of its recombination, which might make a great contribution to the improvement in the photocatalysis efficiency.

In terms of reaction, the h_{pg}^+ can oxidize H$_2$O near the surface of the TiO$_2$ to create hydroxyl radicals (eq 1):

$$h_{pg}^+ + H_2O \rightarrow H^+ + OH^\bullet \tag{1}$$

On the other hand, the e_{pg}^- can reduce O$_2$ to form radicals (O$_2^{\bullet-}$) in eq 2 and further form relatively stable species of H$_2$O$_2$:

$$e_{pg}^- + O_2 \rightarrow O_2^{\bullet-} \tag{2}$$

All these "*in situ*" generated active radicals can degrade the organic molecules present in the medium.

The rather high specific surface area of BiOCl-PT likely provides active sites and allows the reactive molecules to easily diffuse through the pores during photocatalytic degradation. Moreover, the pores present in BiOCl-PT nanocomposite can serve as light-transfer paths for the distribution of photo energy. In this way, the light activation can be enhanced and, in turn, improve the photoabsorption efficiency of the catalyst.

Finally, the photocatalytic activity is closely related to the absorption capacity of the photocatalysts. Thus, the UV−vis diffuse reflectance spectra of PT, BiOCl, and BiOCl-PT were obtained and converted to the visualized absorption spectra shown in Figure 8. The absorption spectra of the three
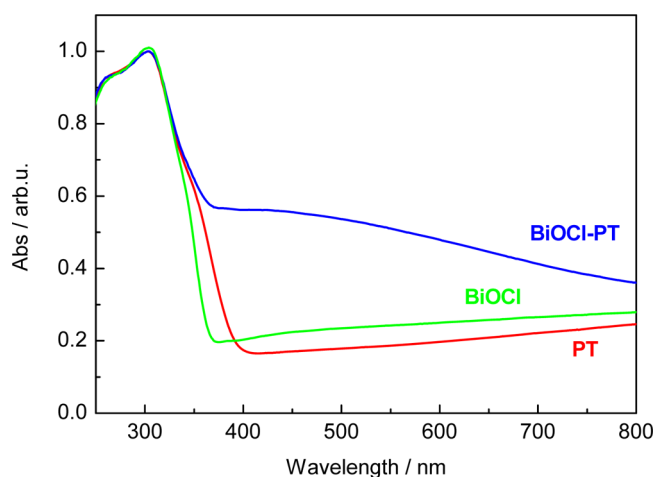

Figure 8. UV−vis absorption spectra of PT (red), BiOCl (green), and BiOCl-PT (blue) photocatalysts.

photocatalysts displayed stepped curves. The absorption spectra of PT and BiOCl exhibit absorption edges at 395 and 360 nm, respectively, from which the absorptions of the photocatalysts sharply decline. On the other hand, the absorption of the BiOCl-PT photocatalyst shows a similar band on the UV range, but the absorption remains >0.5 in the entire UV−vis region. These results indicate that unlike PT and BiOCl, the BiOCl-PT photocatalyst exhibits UV−visible light photoabsorption ability, thus making it a smart candidate as a visible light photocatalyst.

4. CONCLUSIONS

The successful preparation of BiOCl nanoplates inside highly porous TiO$_2$ (BiOCl-PT nanocomposite) has been achieved through a simple sol−gel reaction of tetrabutyl orthotitanate with bismuth(III) chloride. Characterization of the photocatalysts by SEM, HRTEM, XRD, and BET measurements indicated a high degree of porosity as well as a good distribution and high crystallinity of the BiOCl and TiO$_2$ components in the nanocomposite. Aqueous photocatalytic activity tests with RhB under UV−visible light irradiation revealed that BiOCl-PT exhibits a photocatalytic activity higher than those of pure TiO$_2$ and BiOCl components. These new findings prove that combining BiOCl with TiO$_2$ is a convenient strategy for developing highly efficient visible light-responsive photocatalysts and could thus become a smart solution for wastewater treatment.

■ AUTHOR INFORMATION

Corresponding Authors
*E-mail: miguel.guerrero@uab.cat.
*E-mail: egarcia@cidetec.es.
*E-mail: eva.pellicer@uab.cat.

Notes
The authors declare no competing financial interest.

■ REFERENCES

(1) Thompson, T. L.; Yates, J. T., Jr. Surface Science Studies of the Photoactivation of TiO$_2$ New Photochemical Processes. *Chem. Rev.* **2006**, *106*, 4428−4453.
(2) Hoffmann, M. R.; Martin, S. T.; Choi, W.; Bahnemann, D. W. Environmental Applications of Semiconductor Photocatalysis. *Chem. Rev.* **1995**, *95*, 69−96.
(3) Dolbecq, A.; Mialane, P.; Keita, B.; Nadjo, L. Polyoxometalate-based Materials for Efficient Solar and Visible Light Harvesting: Application to the Photocatalytic Degradation of Azo Dyes. *J. Mater. Chem.* **2012**, *22*, 24509−24521.
(4) Fujishima, A.; Honda, K. Electrochemical Photolysis of Water at a Semiconductor Electrode. *Nature* **1972**, *238*, 37−38.
(5) Lazar, M. A.; Varghese, S.; Nair, S. S. Photocatalytic Water Treatment by Titanium Dioxide: Recent Updates. *Catalysts* **2012**, *2*, 572−601.
(6) Jing, J.; Liu, M.; Colvin, V. L.; Li, W.; Yu, W. Band Structure and Photocatalytic Properties of N/Zr co-doped Anatase TiO$_2$ from First-Principles Study. *J. Mol. Catal. A: Chem.* **2011**, *351*, 17−28.
(7) Xiong, Z.; Ma, J.; Ng, W. J.; Waite, T. D.; Zhao, X. S. Silver-Modified Mesoporous TiO$_2$ Photocatalyst for Water Purification. *Water Res.* **2011**, *45*, 2095−2103.
(8) Yu, J.; Wang, B. Effect of Calcination Temperature on Morphology and Photoelectro-chemical Properties of Anodized Titanium Dioxide Nanotube Arrays. *Appl. Catal., B* **2010**, *94*, 295−302.
(9) Devi, L. G.; Kavitha, R. A Review on Non Metal Ion Doped Titania for the Photocatalytic Degradation of Organic Pollutants Under UV/solar Light: Role of Photogenerated Charge Carrier Dynamics in Enhancing the Activity. *Appl. Catal., B* **2013**, *140*, 559−587.
(10) Wang, W. J.; Zhang, L. Z.; An, T. C.; Li, G. Y.; Yipa, H. Y.; Wong, P. K. Comparative Study of Visible-light-driven Photocatalytic Mechanisms of Dye Decolorization and Dacterial Disinfection by B−Ni-codoped TiO$_2$ Microspheres: The Role of Different Reactive Species. *Appl. Catal., B* **2011**, *108*, 108−116.
(11) Teh, C. M.; Mohamed, A. R. Roles of Titanium Dioxide and Ion-doped Titanium Dioxide on Photocatalytic Degradation of Organic Pollutants in Aqueous Solutions: A Review. *J. Alloys Compd.* **2011**, *509*, 1648−1660.
(12) Gang, L.; Wang, X.; Wang, L.; Chen, Z.; Li, F.; Lu, Q. G.; Cheng, H. M. Drastically Enhanced Photocatalytic Activity in Nitrogen Doped Mesoporous TiO$_2$ With Abundant Surface States. *J. Colloid Interface Sci.* **2009**, *334*, 171−175.
(13) Ismail, A. A.; Robben, L.; Bahnemann, D. W. Study of the Efficiency of UV and Visible-Light Photocatalytic Oxidation of

Methanol on Mesoporous RuO_2–TiO_2 Nanocomposites. *ChemPhysChem* **2011**, *12*, 982−991.

(14) Zhang, J.; Xiong, Z.; Zhao, X. S. Graphene−Metal−Oxide Composites for the Degradation of Dyes Under Visible Light Irradiation. *J. Mater. Chem.* **2011**, *21*, 3634−3640.

(15) Ma, J.; Chu, J.; Qiang, L.; Xue, J. J. Synthesis and Structural Characterization of Novel Visible Photocatalyst Bi-TiO_2/SBA-15 and its Photocatalytic Performance. *RSC Adv.* **2012**, *2*, 3753−3758.

(16) Hu, Y.; Cao, Y.; Wang, P.; Li, D.; Chen, W.; He, Y.; Fu, X.; Shao, Y.; Zheng, Y. A New Perspective for Effect of Bi on the Photocatalytic Activity of Bi-doped TiO_2. *Appl. Catal., B* **2012**, *125*, 294−303.

(17) Guerrero, M.; Pané, S.; Nelson, B. J.; Baró, M. D.; Roldán, M.; Sort, J.; Pellicer, E. 3D Hierarchically Porous Cu-BiOCl Nanocomposite Films: One-Step Electrochemical Synthesis, Structural Sharacterization and Nanomechanical and Photoluminescent Properties. *Nanoscale* **2013**, *5*, 12542−12550.

(18) Briand, G. G.; Burford, N. Bismuth Compounds and Preparations with Biological or Medicinal Relevance. *Chem. Rev.* **1999**, *99*, 2601−2658.

(19) Kijima, N.; Matano, K.; Saito, M.; Oikawa, T.; Konishi, T.; Yasuda, H.; Sato, T.; Yoshimura, Y. Oxidative Catalytic Cracking of n-Butane to Lower Alkenes Over Layered BiOCl Catalyst. *Appl. Catal., A* **2001**, *206*, 237−244.

(20) Zhu, L. P.; Liao, G. H.; Bing, N. C.; Wang, L. L.; Yang, Y.; Xie, H. Self-Assembled 3D BiOCl Hierarchitectures: Tunable Synthesis and Characterization. *CrystEngComm* **2010**, *12*, 3791−3796.

(21) Zhang, K.-L.; Liu, C.-M.; Huang, F.-Q.; Zheng, C.; Wang, W.-D. Study of the Electronic Structure and Photocatalytic Activity of the BiOCl Photocatalyst. *Appl. Catal., B* **2006**, *68*, 125−129.

(22) Liu, L.; Zhao, C.; Zhao, H.; Pitts, D.; Li, Y. Porous microspheres of MgO-Patched TiO_2 for CO_2 Photoreduction With H_2O Vapor: Temperature-Dependent Activity and Stability. *Chem. Commun.* **2013**, *49*, 3664−3666.

(23) Kim, W.; Choi, S. Y.; Jeon, Y. M.; Lee, S.; Kim, S. H. Highly-Ordered, Hierarchically Porous TiO_2 Films Via Combination of Two Self-Assembling Templates. *ACS Appl. Mater. Interfaces* **2014**, *6*, 11484−11492.

(24) Wang, X. C.; Yu, J. C.; Ho, C. M.; Hou, Y. D.; Fu, X. Z. Photocatalytic Activity of a Hierarchically Macro/Mesoporous Titania. *Langmuir* **2005**, *21*, 2552−2559.

(25) Joo, J. B.; Dahl, M.; Li, N.; Zaera, F.; Yin, Y. Tailored Synthesis of Mesoporous TiO_2 Hollow Nanostructures for Catalytic Applications. *Energy Environ. Sci.* **2013**, *6*, 2082−2092.

(26) Yang, L.; Si, Z.; Weng, D.; Yao, Y. Synthesis, Characterization and Photocatalytic Activity of Porous WO_3/TiO_2 Microspheres. *Appl. Surf. Sci.* **2014**, DOI: 10.1016/j.apsusc.2014.05.230.

(27) Niedermeier, M. A.; Groß, I.; Müller-Buschbaum, P. Structuring of Titania Thin Films on Different Length Scales Via Combining Block Copolymer Assisted Sol−Gel Templating with Wet-imprinting. *J. Mater. Chem. A* **2013**, *1*, 13399−13403.

(28) Young, R. A. *The Rietveld Method*; Union of Crystallography, Oxford University Press: Oxford, U.K., 1995.

(29) Luterotti, L.; Scardi, P. Simultaneous Structure and Size-strain Refinement by the Rietveld Method. *J. Appl. Crystallogr.* **1990**, *23*, 246−252.

(30) Morales, M.; Chateigner, D.; Luterotti, L. X-ray Textural and Microstructural Characterisations by Using the Combined Analysis Approach for the Optical Optimisation of Micro- and Nano-structured Thin Films. *Thin Solid Films* **2009**, *517*, 6264−6270.

(31) Delhez, R.; de Keijser, Th. H.; Mittemeijer, E. J. Determination of Crystallite Size and Lattice Distortions through X-ray Diffraction Line Profile Analysis. *Fresenius' Z. Anal. Chem.* **1982**, *312*, 1−16.

(32) van Berkum, J. G. M.; Deles, R.; de Keijser, H. Th.; Mittemeijer, E. J. Diffraction-Line Broadening due to Strain Fields in Materials; Fundamental Aspects and Methods of Analysis. *Acta Crystallogr.* **1996**, *A52*, 730−747.

(33) Sort, J.; Suriñach, S.; Muñoz, J. S.; Baró, M. D.; Wojcik, M.; Jedryka, E.; Nadolski, S.; Sheludko, N.; Nogués, J. Role of stacking faults in the structural and magnetic properties of ball-milled cobalt. *Phys. Rev. B* **2003**, *68*, 014421.

(34) Greenwood, N. N.; Earnshaw, A. *Chemistry of the Elements*, 2nd ed.; School of Chemistry, University of Leeds: Leeds, U.K., 1997.

(35) Xie, T. P.; Xu, L. J.; Liu, C. L.; Ding, S. H.; Yang, J.; Wu, W. L. Synthesis and Adsorption Properties of High Specific Surface Area Strontium Ferrite from Industrial Strontium Residue. *Vacuum* **2013**, *93*, 71−78.

(36) Ray, K. J. A.; Viswanathan, B. Effect of Surface Area, Pore Volume and Particle Size of P25 Titania on the Phase Transformation of Anatase to Rutile. *Indian J. Chem.* **2009**, *48A*, 1378−1382.

(37) Chang, X.; Gondal, M. A.; Al-Saadi, A. A.; Ali, M. A.; Shen, H.; Zhou, Q.; Zhang, J.; Du, M.; Liu, Y.; Ji, G. Photodegradation of Rhodamine B Over Unexcited Semiconductor Compounds of BiOCl and BiOBr. *J. Colloid Interface Sci.* **2012**, *377*, 291−298.

(38) Aliabadi, M.; Sagharigar, T. Photocatalytic Removal of Rhodamine B from Aqueous Solutions Using TiO_2 Nanocatalyst. *Journal of Applied Environmental and Biological Sciences* **2001**, *1*, 620−626.

(39) Kong, L.; Jiang, Z.; Lai, H. H. C.; Xiao, T.; Edwards, P. P. Does Noble Metal Modification Improve the Photocatalytic Activity of BiOCl? *Prog. Nat. Sci.* **2013**, *23*, 286−293.

(40) Cai, Y.; Wang, P.; Ye, Y.; Liu, J.; Tian, Z.; Liu, Y.; Liang, C. Grafting BiOCl Nanosheets onto TiO_2 Tubular Arrays to Form a Hierarchical Structure with Improved Photocatalytic Performance. *RSC Adv.* **2013**, *3*, 19064−19069.

(41) You-ji, L.; Wei, C. Photocatalytic Degradation of Rhodamine B Using Nanocrystalline TiO_2-Zeolite Surface Composite Catalysts: Effects of Photocatalytic Condition on Degradation Efficiency. *Catal. Sci. Technol.* **2011**, *1*, 802−809.

(42) Wu, S.; Wang, C.; Cui, Y.; Hao, W.; Wang, T.; Brault, P. BiOCl Nano/Microstructures on Substrates: Synthesis and Photocatalytic Properties. *Mater. Lett.* **2011**, *65*, 1344−1347.

(43) Kang, X.; Chen, S. Photocatalytic Reduction of Methylene Blue by TiO_2 Nanotube Arrays: Effects of TiO_2 Crystalline Phase. *J. Mater. Sci.* **2010**, *45*, 2696−2702.

(44) Liu, Z.; Xu, X.; Fang, J.; Zhu, X.; Li, B. Synergistic Degradation of Eosin Y by Photocatalysis and Electrocatalysis in UV Irradiated Solution Containing Hybrid BiOCl/TiO_2 Particles. *Water, Air, Soil Pollut.* **2012**, *223*, 2783−2798.

(45) Strauss, M.; Pastorello, M.; Sigoli, F. A.; de Souza e Silva, J. M.; Mazali, I. O. Singular Effect of Crystallite Size on the Charge Carrier Generation and Photocatalytic Activity of Nano-TiO_2. *Appl. Surf. Sci.* **2014**, DOI: 10.1016/j.apsusc.2014.06.071.

(46) Kim, D. S.; Han, S. J.; Kwak, S.-Y. Synthesis and Photocatalytic Activity of Mesoporous TiO_2 with the Surface Area, Crystallite Size, and Pore Size. *J. Colloid Interface Sci.* **2007**, *316*, 85−91.

(47) Pare, B.; Sarwan, B.; Jonnlagadda, S. B. Photocatalytic Mineralization Study of Malachite Green on the Surface of Mn-doped BiOCl Activated by Visible Light Under Ambient Condition. *Appl. Surf. Sci.* **2001**, *258*, 247−253.

(48) Cai, Y.; Wang, P.; Ye, Y.; Liu, J.; Tian, Z.; Liu, Y.; Liang, C. Grafting BiOCl Nanosheets onto TiO_2 Tubular Arrays to Form a Hierarchical Structure with Improved Photocatalytic Performance. *RSC Adv.* **2013**, *3*, 19064−19069.